



## Subwavelength Focusing of Bloch Surface Waves

Myun-Sik Kim,<sup>\*,†</sup> Babak Vosoughi Lahijani,<sup>†</sup> Nicolas Deschermes,<sup>†</sup> Jakob Straubel,<sup>‡</sup> Fernando Negredo,<sup>‡</sup> Carsten Rockstuhl,<sup>‡,§</sup> Markus Häyrynen,<sup>||</sup> Markku Kuittinen,<sup>||</sup> Matthieu Roussey,<sup>||</sup> and Hans Peter Herzig<sup>†</sup>

<sup>†</sup>Optics & Photonics Technology Laboratory, Ecole Polytechnique Fédérale de Lausanne (EPFL), Neuchâtel 1015, Switzerland

<sup>‡</sup>Institute of Theoretical Solid State Physics, Karlsruhe Institute of Technology, Karlsruhe 76131, Germany

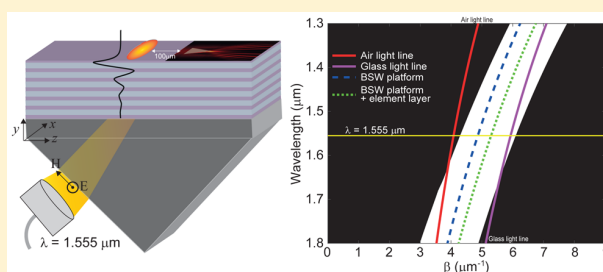
<sup>§</sup>Institute of Nanotechnology, Karlsruhe Institute of Technology, Karlsruhe 76021, Germany

<sup>||</sup>Institute of Photonics, University of Eastern Finland, P.O. Box 111, 80101 Joensuu, Finland

### Supporting Information

**ABSTRACT:** Microsized spheres can focus light into subwavelength spatial domains, a phenomenon called *photonic nanojet*. Even though well studied in three-dimensional (3D) configurations, only a few attempts have been reported to observe similar phenomena in two-dimensional (2D) systems. This, however, is important to take advantage of photonic nanojets in planar optical systems. Usually, surface plasmon polaritons are suggested for this purpose, but they suffer notoriously from rather low propagation lengths due to intrinsic absorption. Here, we solve this problem and explore, numerically and experimentally, the use of Bloch surface waves sustained by a suitably structured all-dielectric media to enable subwavelength focusing in a planar optical system. Since only a low-index contrast can be achieved while relying on Bloch surface waves, we perceive a new functional element that allows a tight focusing and the observation of a photonic nanojet on top of the surface. We experimentally demonstrate a spot size of  $0.66\lambda$  in the effective medium. Our approach paves the way to 2D all-dielectric photonic chips for nanoparticle manipulation in fluidic devices and sensing applications.

**KEYWORDS:** Bloch surface wave (BSW), photonic nanojet, subwavelength focusing, planar optical system, photonic band gap, dispersion relation, funnel device



Two-dimensional surface wave devices are a key asset in the miniaturization of compact optical systems, such as photonic integrated circuits and lab-on-a-chip devices. A frequently studied surface wave is the surface plasmon polariton (SPP), which propagates along the interface between a dielectric and a metal.<sup>1</sup> Since the field of SPPs is partially localized in the metal, SPPs are limited in their propagation length by the dissipation. This constitutes a severe limitation for many existing and potential applications, in particular, in planar photonic devices. In that point of view, surface waves sustained by all-dielectric media are much more appealing because they do not suffer from dissipation.

Two dielectric surface waves are known by now. One is called the Dyakonov wave, in reference to M. I. Dyakonov, who made the first prediction.<sup>2</sup> It is a surface wave that propagates at the interface between two dielectric media where at least one of the two media should be anisotropic.<sup>3</sup> This requirement limits the fabrication possibilities and also the application perspective. The second is called a Bloch surface wave (BSW).<sup>4</sup> Electromagnetic surface modes can be sustained by photonic crystals of different dimensions.<sup>5</sup> BSWs are a particular case supported at the edge of a truncated one-dimensional (1D) periodic dielectric media, i.e., a dielectric multilayer serving as 1D

photonic crystals.<sup>5,6</sup> BSWs are sustained in the frequency region of the localized photonic band gap. The band gap denies propagation into the half-space containing the multilayer structure. Since the propagation constant of the mode is outside the light cone of the medium in the other half-space, a surface mode is supported. At the edge of the truncated 1D photonic crystal, the thickness of the terminating layer is usually suitably tuned to let the BSW propagate at a frequency central to the band gap of the 1D photonic crystal. This improves its confinement. This last layer is called the defect layer. In an experiment, however, the finiteness of the multilayer structure causes some radiation losses. That finite radiation loss is also important to excite BSWs by means of frustrated total internal reflection. Since BSWs can reside between isotropic dielectric media, their choice of materials and fabrication is much more flexible, and a wide range of ambient materials are allowed. In addition, the use of lossless dielectric media guarantees a long propagation length. For instance, a BSW with a propagation length of 3.24 mm at  $\lambda = 1.558 \mu\text{m}$  has been reported.<sup>7</sup> Such

**Received:** March 13, 2017

**Published:** May 16, 2017

promising characteristics of BSWs have inspired various studies in recent years. Devices with basic functionalities have been explored, e.g., a prism demonstrating refraction of the propagating surface wave,<sup>8</sup> a grating for the generation of two-dimensional (2D) Talbot images on the multilayer surface,<sup>8</sup> plano-convex<sup>9</sup> and double-convex<sup>10</sup> lenses, and waveguide components.<sup>11–13</sup> All these elements came within reach by adding a structured element layer on top of the stratified media. This locally changes the dispersion relation of the BSW and allows controlling the way it propagates. More advanced functionalities have also been investigated, e.g., linear<sup>14</sup> and circular<sup>15</sup> grating couplers that couple the surface waves without a prism coupling setup like the Kretschmann configuration.<sup>16</sup> Furthermore, the research has been extended to demonstrate applications for enhanced fluorescence detection,<sup>15</sup> resonators,<sup>17</sup> and biosensing.<sup>18–21</sup> However, one of the most essential functionalities of an optical system, a tight focusing, turned out to be nontrivial and has not yet been reported. It can be explained by the rather limited effective refractive index contrast ( $\Delta n$ ) of the BSW sustained by the multilayer platforms when considered with and without the element layer. For fixed designs of focusing elements, the optical power mainly depends on  $\Delta n$  according to the lens maker's formula. In conventional optical systems, e.g., those based on air and glass systems, the index contrast is approximately 0.5, whereas for most dielectric surface waves the index contrast is only on the order of 0.1. This causes a weaker optical power when conventional component designs are applied to the BSWs.<sup>9,10</sup> In this paper, we mitigate this problem and investigate a component design that realizes a better spatial confinement of Bloch surface waves while fully respecting the intrinsic limitations imposed by the low-index contrast.

A prime example of tight focusing using a simple component is the scattering of plane waves at dielectric microspheres. The Mie scattering effect assists in generating a highly confined beam, named a photonic nanojet,<sup>22</sup> which propagates over several wavelengths while maintaining a subwavelength beam size, e.g., a full width at half-maximum (fwhm) spot size smaller than one-half of the wavelength for optimal conditions of the refractive index contrast and the size of the sphere with respect to the wavelength. Like this, such a simple element, i.e., a microsphere, serves as the highest NA focusing lens in air. Most appealing of photonic nanojets is their support of various super-resolution applications, e.g., nanolithography,<sup>23</sup> single-molecule sensing,<sup>24</sup> nanoparticle detection,<sup>25</sup> and super-resolution imaging systems.<sup>26–29</sup> Photonics nanojet components are also suitable for integrated photonic systems. For instance, a sphere sustaining a photonic nanojet can be integrated with a focal plane array detector, enhancing the measured signal.<sup>30</sup> Microsphere chains can also perform periodic focusing<sup>31</sup> and polarization control.<sup>32</sup> The majority of photonic nanojet studies are devoted to 3D systems. For 2D systems, surface plasmon polariton devices have been applied to attempt a tight focusing; for example, a gradient-index lens<sup>33</sup> and SPP photonic nanojets were generated on metal surfaces.<sup>34,35</sup> However, dielectric surface wave devices have not yet allowed such a tight focusing. We approach this challenge here by developing new components enabling focusing Bloch surface waves to subwavelength domains. Emphasis is put on studying the influence of the low-index contrast on the photonic nanojet focusing and how to circumvent the weaker focusing using an alternative geometry. We are driven by the idea of avoiding

complexity in the design and small feature sizes to continue to rely on standard fabrication processes.

In previous works,<sup>7–9</sup> multilayer platforms for the Bloch surface wave have been established from visible to near-infrared (IR) wavelengths. Here, a BSW platform operating at near-IR frequencies has been employed. The near-field distribution of a selected device has been measured with a custom scanning near-field optical microscope (SNOM). Effective modeling using a simplified 2D system and full-wave numerical 3D simulations of the actual structure provide further insights. We stress the fact that even though demonstrated here at a specific operational frequency, the scalability of Maxwell's equations allows the easy extrapolation of all observed effects to different spectral regions, as long as materials with suitable dielectric properties are available.

## METHODS AND EXPERIMENTAL DETAILS

Figure 1 shows a schematic of our experimental setup. It includes the multilayer structures, a Kretschmann coupling

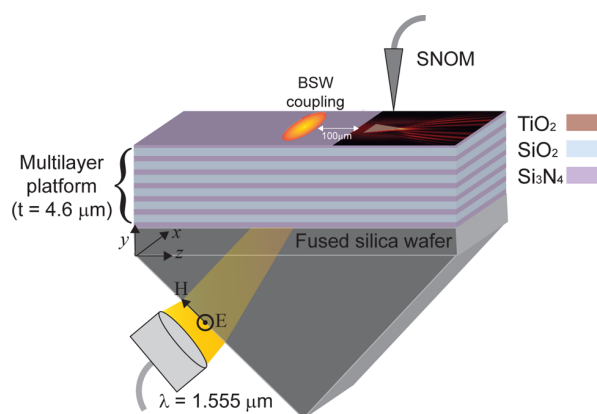


**Figure 1.** Schematic drawing of the experimental setup including the multilayer structure, Kretschmann coupling configuration, and the SNOM probe for near-field measurements. The multilayer platform consists of six periods of a layer made from  $\text{Si}_3\text{N}_4$  and from  $\text{SiO}_2$  with a thickness of 283 and 472 nm, respectively. A  $\text{Si}_3\text{N}_4$  defect layer was deposited on top with a thickness of 50 nm. The element layer is 47 nm thick and made from  $\text{TiO}_2$ . This layer is patterned to form the focusing element.

configuration, and the SNOM probe. For the illumination we use a free space wavelength of  $\lambda = 1.555 \mu\text{m}$ .

The polarization is transverse electric (TE). The multilayer design has been conducted by calculating the band gap diagram and dispersion curves using a transfer matrix method<sup>6</sup> and a numerical eigenmode solver, CAMFR.<sup>36</sup> The designed multilayer stack consists of six periods of silicon nitride ( $\text{Si}_3\text{N}_4$ ,  $n_{\text{Si}_3\text{N}_4} = 1.94$ ,  $t = 283 \text{ nm}$ ) and silicon dioxide ( $\text{SiO}_2$ ,  $n_{\text{SiO}_2} = 1.47$ ,  $t = 472 \text{ nm}$ ), where  $t$  is thickness. An additional 50 nm thick layer of  $\text{Si}_3\text{N}_4$  is deposited on top of the periodic layers as a defect layer. The element layer is a 47 nm thick titanium dioxide layer ( $\text{TiO}_2$ ,  $n_{\text{TiO}_2} = 2.23$ ), which is patterned to form the focusing element. The total thickness of the multilayer stack is approximately  $t = 4.6 \mu\text{m}$ .

The dispersion curves with corresponding band gap diagram of the current chip design is shown in Figure 2a. The field distribution throughout the multilayers at the operational wavelength of  $1.555 \mu\text{m}$  is shown by the real part of the complex electric field in Figure 2b, which verifies the efficient

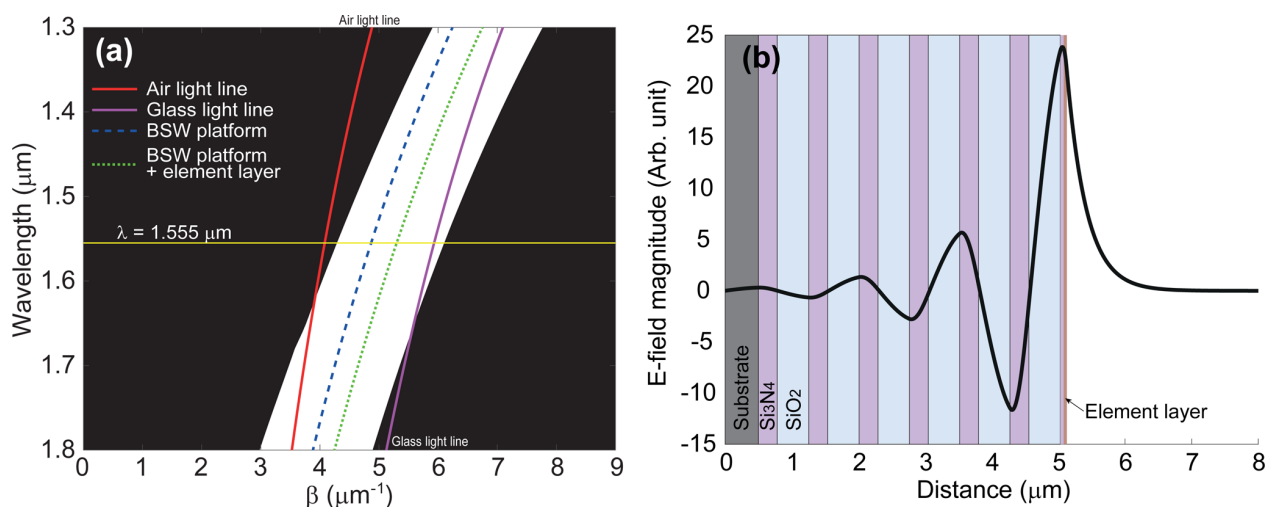


**Figure 2.** (a) Dispersion curves of the designed multilayer platform with/without the element layer and the band gap diagram (the clear area is the localized photonic band gap). (b) Electric field profile (i.e., the real part of the complex electric field) of the BSW throughout the multilayer structures at the operational wavelength of 1.555  $\mu\text{m}$ .

confinement of the BSW. The mode can be, however, excited by means of frustrated total internal reflection through the glass prism as performed in the Kretschmann configuration. Increasing the thickness of the defect layer causes the dispersion line to move toward the band edge near the glass light line. When adding the 47 nm thick element layer made from  $\text{TiO}_2$  on top of the multilayer platform (1D photonic crystal + defect layer), the dispersion curve of the entire system shifts further to the glass light line.

For the operational wavelength, the dispersion curves of the platforms with/without the element layer causes an effective refractive index difference, as shown in Figure 2a by blue dashed and green dotted lines within the band gap. The effective refractive index of the BSW is defined by  $n_{\text{BSW}} = c\beta/\omega$ , where  $c$  is the speed of light in a vacuum,  $\omega$  is the angular frequency, and  $\beta = k \sin \theta$  is the wavenumber of the surface mode with  $k$  the wavenumber in the glass substrate and  $\theta$  the incident angle in the Kretschmann configuration.<sup>9</sup> From Figure 2a, the effective refractive indices of the platform with and without the element layer can be extracted as  $n_{\text{eff1}} = 1.3$  and  $n_{\text{eff2}} = 1.2$ , respectively, resulting in an index contrast  $\Delta n_{\text{eff}} = 0.1$ . Accordingly, the effective wavelength of the BSW ( $\lambda_{\text{BSW}}$ ) propagating on the multilayer platform without the element layer is the free space wavelength times the reciprocal of  $n_{\text{eff2}}$ . The band gap and the substrate dispersion line limit the maximum index contrast. In the current platform, the maximum  $\Delta n_{\text{eff}}$  of 0.23 can be achieved by an element layer ( $\text{TiO}_2$ ) thickness of 100 nm. For experimental convenience and flexibility, the actual device is designed to have the dispersion curve close to the middle of the photonic band gap. In theory and while ignoring other restrictions of fabrications and coupling conditions, high-index substrate materials, e.g., amorphous silicon with an  $n = 3.48$ , can expand the  $\Delta n_{\text{eff}}$  up to approximately 0.38 with a similar multilayer stack design. Nevertheless, it is impossible to achieve the optimal index contrast for the conventional photonic nanojet generation. The location and intensity of photonic nanojets strongly depend on the refractive index contrast between the sphere and its surrounding medium, as well as its size. Since there is no basic relation, the accurate location and spot size of photonic

nanojets are usually obtained by rigorous numerical methods,<sup>22,37</sup> where the optimal index contrast to acquire a subwavelength spot size is found to be in the range between 0.5 and 1.

Since the index contrast of the BSW systems does not meet the optimal conditions for the conventional photonic nanojet based on spherical geometries, alternative designs have to be found to squeeze the light into subwavelength spatial domains. It is known that noncircular shapes, for instance, pyramid shapes<sup>38</sup> or square pillars,<sup>39</sup> can generate photonic nanojet spots as well. Therefore, we explored such elements. We consider standard fabrication processes by avoiding small feature sizes and fixed the critical dimensions of the considered structure to 10  $\mu\text{m}$ . Structures with these dimensions can be easily patterned by conventional lithographic methods. Avoiding complex designs, we investigate simple geometries, such as circle, ellipse, and triangle. The performance of each geometry has been assessed by studying at first the light propagation numerically. Preliminary simulations were based on fast and resource-efficient 2D simulations. For the final design, selected full 3D simulations considering the exact geometry were done. All simulations have been performed using a commercial time domain solver that is based on the finite integration technique as implemented in CST Microwave Studio. In the preliminary 2D simulations, we consider a scalar situation and light propagation in a medium characterized by only the effective refractive indices of the focusing element and the effective surrounding medium. We do not include the multilayer stacks as is done in full 3D modeling. This 2D model mimics the propagation of the BSW along the surface.

## RESULTS AND DISCUSSION

We first verify how much we can reduce the focal spot by elongating the conventional circular design to a prolate ellipse (see Supporting Information). The axis length of the ellipse in one dimension was considered as the critical dimension of the structure and was fixed to 10  $\mu\text{m}$ . The second axis length of the ellipse was changed from 10  $\mu\text{m}$  to 25  $\mu\text{m}$  with an interval of 5  $\mu\text{m}$ . However, the low-index contrast ( $\Delta n_{\text{eff}} = 0.1$ ) forces the circular and prolate ellipse designs to act rather as a double



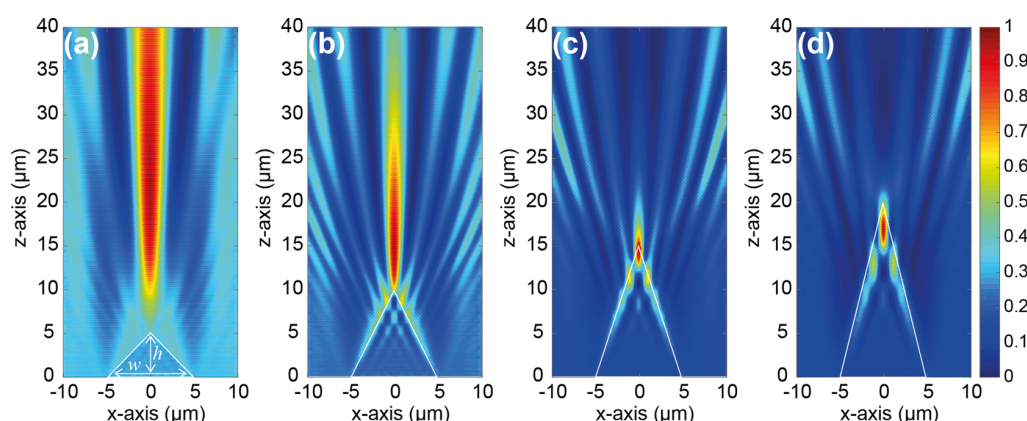


**Figure 3.** 2D simulation results of the intensity distributions, at  $\lambda = 1.555 \mu\text{m}$ , for photonic nanojet devices for BSWs based on isosceles triangles. While the base of  $w = 10 \mu\text{m}$  has been fixed and the height  $h$  varied from 5 to 20  $\mu\text{m}$ , (a–d)  $h = 5, 10, 15, 20 \mu\text{m}$ , respectively. (c) For the aspect ratio  $h/w$  equal to 1.5, the best confinement is obtained, where the fwhm spot size equals  $0.73\lambda_{\text{BSW}}$ . (d) When the aspect ratio further increases, the focal spot is buried in the element. The intensity is normalized to the maximum of each figure.

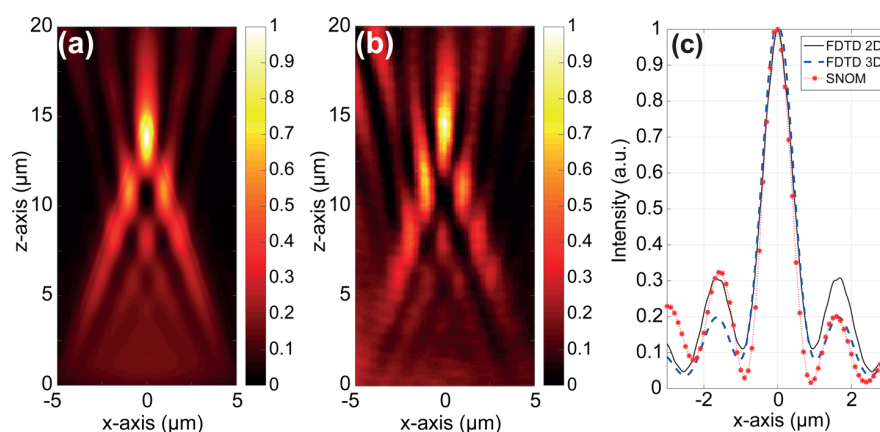


**Figure 4.** (a) 3D simulation result for the  $x$ – $z$  intensity (that is, electric field amplitude squared) distribution. (b) Measured near-field intensity distribution of the fabricated funnel device. (c)  $x$ -Axis profiles at  $z = 15 \mu\text{m}$  of the 2D (dark solid line) and the 3D (blue dashed line) simulations, and the measured intensity (red dotted-asterisk line). Results are extracted from Figures 3c and Figure 4a and b, respectively.

convex lens and do not yield a photonic nanojet. A small refraction angle from the illumination-side surface lowers the numerical aperture (NA) of the system, and a tight focusing was not observed. Therefore, the confinement of light in the focal spot was weaker than that of conventional photonic nanojets. For instance, the smallest focal spot with an elliptical design, shown in the Supporting Information in Figure S1(d), has a fwhm size of  $1.25 \mu\text{m}$ , which is approximately  $0.96\lambda_{\text{BSW}}$ . This is far away from the typical spot size of a conventional photonic nanojet, i.e., slightly larger than half the wavelength.

To further enhance the light confinement toward a subwavelength size, we introduce a noncircular design and consider an isosceles triangle. With such a geometry, we return eventually to the prototypical structure that allows inducing diffraction-free beams in a 2D geometry. The isosceles triangle introduces two spatial frequencies that are linked to the index contrast and the geometrical dimensions. These two plane waves share the same propagation constant and have oppositely signed wave vector components in the transverse direction. They interfere and eventually cause a standing wave pattern that is invariant along the propagation direction. The finiteness of the isosceles triangle limits, obviously, the spatial extent where the beam is diffraction free, comparable to the design

constraints of an axicon. By changing the height of the isosceles triangle we can change the spatial extent in which the beam is free of diffraction, limiting it closer to the top of the triangle. The two counter-propagating waves, in the limiting case, can be focused to exactly half a wavelength, which promises to obtain a spatial localization of the field close to the tip of the triangle approaching this fundamental lower bound. This design approach has been first numerically investigated using 2D simulations. In our analysis we fixed the width  $w$  to be  $10 \mu\text{m}$  and varied the height  $h$  of the isosceles triangle from  $5 \mu\text{m}$  to  $20 \mu\text{m}$  with an interval of  $5 \mu\text{m}$ .

Figure 3 shows the intensity distributions of 2D simulation results for different aspect ratios ( $h/w$ ). Note that the intensity is the square of the electric field amplitude and the incidence is the  $x$ -polarized plane wave in these 2D simulations. When the  $h/w$  ratio grows, the focal spot gradually becomes smaller until it is buried in the element (see Figure 3d). The best confinement is found for  $h/w = 1.5$ , as shown in Figure 3c. Similar to the photonic nanojet spots, the focal spot arises just at the top of the isosceles triangle. The fwhm spot size reaches  $950 \text{ nm}$ , i.e.,  $0.73\lambda_{\text{BSW}}$ . This behavior is in agreement with the physical understanding developed above. For a shallow height, the induced transverse momentum given to the two plane

waves is quite small. This causes the modulation of the intensity in the transverse direction to be spatially extended; that is, there is no tight focusing. Increasing the height will increase the induced transverse momentum. This squeezes the spatial extent. But the structure is neither infinitely extended nor periodically arranged. This limits the extension in the propagation direction in which the beam can be considered as free of diffraction; it restricts the longitudinal size of the photonic nanojet. Numerically we observe that an optimum is met at the ratio of  $h/w = 1.5$ . There, a tight focusing above the tip of the triangle is obtained. This optimum design eventually is the structure we are looking at in the experiments described further below.

For this final design, studied in Figure 3c, we also apply a full 3D simulation as described above to verify the validity of the 2D results (for details see the Supporting Information). The results of the 3D simulations are shown in Figure 4 along with the experimental results for comparison.

For the experimental verification, we have fabricated the funnel device whose field has been studied in Figure 3c, i.e., the isosceles triangle of  $w = 10 \mu\text{m}$  and  $h = 15 \mu\text{m}$  in the element layer. Multilayers of  $\text{Si}_3\text{N}_4$  and  $\text{SiO}_2$  are deposited by using plasma-enhanced chemical vapor deposition (PECVD) on a fused silica wafer. The element ( $\text{TiO}_2$ ) layer was deposited by atomic layer deposition (ALD). The patterning of the  $\text{TiO}_2$  layer was performed by electron-beam lithography (EBL) and subsequent inductively coupled plasma reactive ion etching (ICP-RIE) processes. The details of the fabrication can be found in Supporting Information.

Using the Kretschmann coupling configuration shown in Figure 1, the incident laser beam with TE polarization and a free space wavelength of  $\lambda = 1.555 \mu\text{m}$  is successfully coupled to the top of the multilayer  $100 \mu\text{m}$  away from the fabricated isosceles triangle element. The illumination is a weakly focused Gaussian beam with a fwhm size of  $25 \mu\text{m}$ . Since it is coupled at the focal plane of the illumination lens, the propagating surface wave exhibits a planar wavefront that is not diverging. This imitates a collimated beam bound to the surface, which is the experimental counterpart of the plane wave illumination considered in the simulation. The SNOM setup employs a commercial metal-coated fiber tip ( $200 \text{ nm}$  aperture) to scan over the funnel device. A scan in the  $xz$ -plane over a spatial region of  $10 \mu\text{m}$  by  $20 \mu\text{m}$  with a scan step of  $100 \text{ nm}$  in both directions has been performed. Figure 4b shows the measured near-field intensity distribution. It shows an excellent agreement with the numerical results shown in Figures 3c and 4a corresponding to the 2D and 3D simulations, respectively. For further analysis, we extract and plot the intensity profiles at  $z = 15 \mu\text{m}$  along the  $x$ -axis from numerical and experimental results. The direct comparison is shown in Figure 4c, where all profiles are normalized to have the same peak value. Except the negligible deviations in the side lobes, the main lobe profile shows an excellent match. The measured fwhm spot size is  $858 \text{ nm}$ , i.e.,  $0.66\lambda_{\text{BSW}}$ . Fabrication and experimental errors, such as an alignment error and imperfect illumination conditions, may cause the deviations in the side lobes.

## CONCLUSIONS

We have investigated numerically and experimentally how to focus Bloch surface waves into a subwavelength spatial domain using a near-IR free space wavelength  $\lambda = 1.555 \mu\text{m}$ . We considered a simple component such as a microsphere that generates a subwavelength focus via the photonic nanojet effect.

However, the available material platforms to host the BSW provide as an intrinsic limitation only a rather low index contrast ( $\Delta n_{\text{eff}} = 0.1$  for the current multilayer design) to steer the propagation of the BSW. This denies achieving the optimal index contrast condition for the conventional photonic nanojet that requires a  $\Delta n$  to be in the range of 0.5 to 1. By means of simplified 2D simulations, it has been demonstrated that circular and elliptical designs do not provide spot sizes comparably small to those of conventional photonic nanojets. To enhance the spatial confinement, we suggested a novel device concept that relies on an isosceles triangle. It introduces two spatial frequencies that cause a pattern free of diffraction for a shallow height that is, however, not strongly localized in space. Increasing the height of the isosceles triangle enhances the localization but lowers simultaneously the diffraction free extent of the propagation direction. The optimal design has been obtained by an isosceles triangle of the width  $w = 10 \mu\text{m}$  and the height  $h = 15 \mu\text{m}$ . For this final design, a full 3D simulation verifies the validity of 2D simplified simulation results. By using a SNOM measurement, we experimentally verify the performance of the fabricated device, demonstrating an fwhm spot size of  $858 \text{ nm}$  ( $= 0.66\lambda_{\text{BSW}}$ ). Considering fabrication and experimental deviations, the results show an excellent agreement with the 2D and 3D simulation results.

Thanks to their all-dielectric nature, BSW platforms pave the way for planar photonic systems with very large propagation lengths. The demonstrated subwavelength focusing of the surface waves can fill the vacancy of the BSW components for single-molecule sensing,<sup>24</sup> nanoparticle detection,<sup>25,40</sup> trapping and sensing,<sup>41–43</sup> and all-optical switching.<sup>44</sup> In order to provide solid perspectives for such applications, a numerical demonstration of nanoparticle detection is presented in the Supporting Information (see Section 4).

## ASSOCIATED CONTENT

### Supporting Information

The Supporting Information is available free of charge on the ACS Publications website at DOI: 10.1021/acsphotonics.7b00245.

2D simulation results of conventional photonic nanojet device designs (i.e., circular and ellipse), 3D simulation details, fabrication details, and numerical demonstration of nanoparticle detection (PDF)

## AUTHOR INFORMATION

### Corresponding Author

\*E-mail: myun-sik.kim@epfl.ch.

### ORCID

Myun-Sik Kim: 0000-0002-7795-3622

### Notes

The authors declare no competing financial interest.

## ACKNOWLEDGMENTS

This research is supported by the Swiss National Science Foundation (SNSF FN200020-135455), Finnish Funding Agency for Innovation (Project Tekes) FiDiPro NP-NANO (40315/13), and the Deutsche Forschungsgemeinschaft (DFG) through CRC 1173. J.S. and F.N. also acknowledge support from the Karlsruhe School of Optics and Photonics (KSOP).

## REFERENCES

- (1) Raether, H. *Surface Plasmons on Smooth and Rough Surfaces and on Gratings*; Springer: New York, 1988.
- (2) Dyakonov, M. I. New type of electromagnetic wave propagating at an interface. *J. Exp. Theor. Phys.* **1988**, *67*, 714–716.
- (3) Takayama, O.; Artigas, D.; Torner, L. Lossless directional guiding of light in dielectric nanosheets using Dyakonov surface waves. *Nat. Nanotechnol.* **2014**, *9*, 419–424.
- (4) Bloch, F. Über die Quantenmechanik der Elektronen in Kristallgittern. *Eur. Phys. J. A* **1928**, *52*, 555–600.
- (5) Angelini, A. *Photon Management Assisted by Surface Waves on Photonic Crystals*; Springer: New York, 2017.
- (6) Yeh, P.; Yariv, A.; Hong, C.-S. Electromagnetic propagation in periodic stratified media. I. General theory. *J. Opt. Soc. Am.* **1977**, *67*, 423–438.
- (7) Dubey, R.; Barakat, E.; Häyrynen, M.; Roussey, M.; Honkanen, S. K.; Kuittinen, M.; Herzig, H. P. Experimental investigation of the propagation properties of Bloch surface waves on dielectric multilayer platform. *J. Eur. Opt. Soc. Rapid Publ.* **2017**, *13*, 5.
- (8) Yu, L.; Barakat, E.; Di Francesco, J.; Herzig, H. P. Two-dimensional polymer grating and prism on Bloch surface waves platform. *Opt. Express* **2015**, *23*, 31640–31647.
- (9) Yu, L.; Barakat, E.; Sfez, T.; Hvozdar, L.; Di Francesco, J.; Herzig, H. P. Manipulating Bloch surface waves in 2D: a platform concept-based flat lens. *Light: Sci. Appl.* **2014**, *3*, e124.
- (10) Angelini, A.; Lamberti, A.; Ricciardi, S.; Frascella, F.; Munzert, P.; De Leo, N.; Descrovi, E. In-plane 2D focusing of surface waves by ultrathin refractive structures. *Opt. Lett.* **2014**, *39*, 6391–6394.
- (11) Sfez, T.; Descrovi, E.; Yu, L.; Quaglio, M.; Dominici, L.; Nakagawa, W.; Michelotti, F.; Giorgis, F.; Herzig, H. P. Two-dimensional optics on silicon nitride multilayer: Refraction of Bloch surface waves. *Appl. Phys. Lett.* **2010**, *96*, 151101.
- (12) Descrovi, E.; Sfez, T.; Quaglio, M.; Brunazzo, D.; Dominici, L.; Michelotti, F.; Herzig, H. P.; Martin, O. J. F.; Giorgis, F. Guided Bloch Surface Waves on Ultrathin Polymeric Ridges. *Nano Lett.* **2010**, *10*, 2087–2091.
- (13) Yu, L.; Barakat, E.; Nakagawa, W.; Herzig, H. P. Investigation of ultra-thin waveguide arrays on a Bloch surface wave platform. *J. Opt. Soc. Am. B* **2014**, *31*, 2996–3000.
- (14) Descrovi, E.; Barakat, E.; Angelini, A.; Munzert, P.; De Leo, N.; Boarino, L.; Giorgis, F.; Herzig, H. P. Leakage radiation interference microscopy. *Opt. Lett.* **2013**, *38*, 3374–3376.
- (15) Angelini, A.; Barakat, E.; Munzert, P.; Boarino, L.; De Leo, N.; Enrico, E.; Giorgis, F.; Herzig, H. P.; Pirri, C. F.; Descrovi, E. Focusing and Extraction of Light mediated by Bloch Surface Waves. *Sci. Rep.* **2015**, *4*, 5428.
- (16) Kretschmann, E.; Raether, H. Radiative decay of nonradiative surface plasmons excited by light. *Z. Naturforsch., A: Phys. Sci.* **1968**, *23*, 2135–2136.
- (17) Dubey, R.; Vosoughi Lahijani, B.; Barakat, E.; Häyrynen, M.; Roussey, M.; Kuittinen, M.; Herzig, H. P. Near-field characterization of a Bloch-surface-wave-based 2D disk resonator. *Opt. Lett.* **2016**, *41*, 4867–4870.
- (18) Santi, S.; Musi, V.; Descrovi, E.; Paeder, V.; Di Francesco, J.; Hvozdar, L.; van der Wal, P.; Lashuel, H. A.; Pastore, A.; Neier, R.; Herzig, H. P. Real-time Amyloid Aggregation Monitoring with a Photonic Crystal-based Approach. *ChemPhysChem* **2013**, *14*, 3476–3482.
- (19) Toma, K.; Descrovi, E.; Toma, T.; Ballarini, M.; Mandracchi, P.; Giorgis, F.; Mateescu, A.; Jonas, U.; Knoll, W.; Dostálek, J. Bloch surface wave-enhanced fluorescence biosensor. *Biosens. Bioelectron.* **2013**, *43*, 108–114.
- (20) Frascella, F.; Ricciardi, S.; Rivolo, P.; Moi, V.; Giorgis, F.; Descrovi, E.; Michelotti, F.; Munzert, P.; Danz, N.; Napione, L.; Alvaro, M.; Bussolino, F. A Fluorescent One-Dimensional Photonic Crystal for Label-Free Biosensing Based on Bloch Surface Waves. *Sensors* **2013**, *13*, 2011–2022.
- (21) Sinibaldi, A.; Danz, N.; Anopchenko, A.; Munzert, P.; Schmieder, S.; Chandrawati, R.; Rizzo, R.; Rana, S.; Sonntag, F.; Occhicone, A.; Napione, L.; De Panfilis, S.; Stevens, M. M.; Michelotti, F. Label-Free Detection of Tumor Angiogenesis Biomarker Angiopoietin 2 Using Bloch Surface Waves on One Dimensional Photonic Crystals. *J. Lightwave Technol.* **2015**, *33*, 3385–3393.
- (22) Heifetz, A.; Kong, S.-C.; Sahakian, A. V.; Taflove, A.; Backman, V. Photonic nanojets. *J. Comput. Theor. Nanosci.* **2009**, *6*, 1979–1992.
- (23) McLeod, E.; Arnold, C. B. Subwavelength direct-write nanopatterning using optically trapped microspheres. *Nat. Nanotechnol.* **2008**, *3*, 413–417.
- (24) Gérard, D.; Wenger, J.; Devilez, A.; Gachet, D.; Stout, B.; Bonod, N.; Popov, E.; Rigneault, H. Strong electromagnetic confinement near dielectric microspheres to enhance single-molecule fluorescence. *Opt. Express* **2008**, *16*, 15297–15303.
- (25) Yang, H.; Cornaglia, M.; Gijs, M. A. M. Photonic Nanojet Array for Fast Detection of Single Nanoparticles in a Flow. *Nano Lett.* **2015**, *15*, 1730–1735.
- (26) Krivitsky, L. A.; Wang, J. J.; Wang, Z.; Luk'yanchuk, B. Locomotion of microspheres for super-resolution imaging. *Sci. Rep.* **2013**, *3*, 3501.
- (27) Allen, K. W.; Farahi, N.; Li, Y.; Limberopoulos, N. I.; Walker, D. E., Jr.; Urbas, A. M.; Liberman, V.; Astratov, V. N. Super-resolution microscopy by movable thin-films with embedded microspheres: Resolution analysis. *Ann. Phys. (Berlin, Ger.)* **2015**, *527*, 513–522.
- (28) Monks, J. N.; Yan, B.; Hawkins, N.; Vollrath, F.; Wang, Z. Spider Silk: Mother Nature's Bio-Superlens. *Nano Lett.* **2016**, *16*, 5842–5845.
- (29) Yang, H.; Trouillon, R.; Huszka, G.; Gijs, M. A. M. Super-Resolution Imaging of a Dielectric Microsphere Is Governed by the Waist of Its Photonic Nanojet. *Nano Lett.* **2016**, *16*, 4862–4870.
- (30) Allen, K. W.; Abolmaali, F.; Duran, J. M.; Ariyawansa, G.; Limberopoulos, N. I.; Urbas, A. M.; Astratov, V. N. Increasing sensitivity and angle-of-view of mid-wave infrared detectors by integration with dielectric microspheres. *Appl. Phys. Lett.* **2016**, *108*, 241108.
- (31) Allen, K. W.; Darafsheh, A.; Abolmaali, F.; Mojaverian, N.; Limberopoulos, N. I.; Lupu, A.; Astratov, V. N. Microsphere-chain waveguides: Focusing and transport properties. *Appl. Phys. Lett.* **2014**, *105*, 021112.
- (32) Darafsheh, A.; Mojaverian, N.; Limberopoulos, N. I.; Allen, K. W.; Lupu, A.; Astratov, V. N. Formation of polarized beams in chains of dielectric spheres and cylinders. *Opt. Lett.* **2013**, *38*, 4208–4211.
- (33) Zentgraf, T.; Liu, Y.; Mikkelsen, M. H.; Valentine, J.; Zhang, X. Plasmonic Luneburg and Eaton lenses. *Nat. Nanotechnol.* **2011**, *6*, 151–155.
- (34) Ju, D.; Pei, H.; Jiang, Y.; Sun, X. Controllable and enhanced nanojet effects excited by surface plasmon polariton. *Appl. Phys. Lett.* **2013**, *102*, 171109.
- (35) Khaleque, A.; Li, Z. Tailoring the Properties of Photonic Nanojets by Changing the Material and Geometry of the Concentrator. *Prog. Electromagn. Res. Lett.* **2014**, *48*, 7–13.
- (36) CAMFR: <http://camfr.sourceforge.net/>.
- (37) Lee, S.; Li, L.; Wang, Z. Optical resonances in microsphere photonic nanojets. *J. Opt.* **2016**, *16*, 015704.
- (38) Martin, J.; Proust, J.; Gérard, D.; Bijeon, J.-L.; Plain, J. Intense Bessel-like beams arising from pyramid-shaped microtips. *Opt. Lett.* **2012**, *37*, 274–276.
- (39) Kotlyar, V. V.; Stafeev, S. S.; Feldman, A. Photonic nanojets generated using square-profile microsteps. *Appl. Opt.* **2014**, *53*, S322–S329.
- (40) Juan, M. L.; Righini, M.; Quidant, R. Plasmon nano-optical tweezers. *Nat. Photonics* **2011**, *5*, 349–356.
- (41) Li, X.; Chen, Z.; Taflove, A.; Backman, V. Optical analysis of nanoparticles via enhanced backscattering facilitated by 3-D photonic nanojets. *Opt. Express* **2005**, *13*, 526–533.
- (42) Lin, S.; Zhu, W.; Jinand, Y.; Crozier, K. B. Surface-Enhanced Raman Scattering with Ag Nanoparticles Optically Trapped by a Photonic Crystal Cavity. *Nano Lett.* **2013**, *13*, 559–563.

(43) Li, Y.; Xin, H.; Liu, X.; Zhang, Y.; Lei, H.; Li, B. Trapping and Detection of Nanoparticles and Cells Using a Parallel Photonic Nanojet Array. *ACS Nano* **2016**, *10*, 5800–5808.

(44) Born, B.; Geoffroy-Gagnon, S.; Krupa, J. D. A.; Hristovski, I. R.; Collier, C. M.; Holzman, J. F. Ultrafast All-Optical Switching via Subdiffractional Photonic Nanojets and Select Semiconductor Nanoparticles. *ACS Photonics* **2016**, *3*, 1095–1101.